THE ASTROPHYSICAL JOURNAL, 527:86–101, 1999 December 10

A COMPACT CYLINDRICAL GREEN'S FUNCTION EXPANSION FOR THE SOLUTION OF POTENTIAL PROBLEMS

HOWARD S. COHL AND JOEL E. TOHLINE
Department of Physics and Astronomy, Louisiana State University, Baton Rouge, LA 70803
Received 1999 February 5; accepted 1999 July 22

ABSTRACT

We show that an exact expression for the Green's function in cylindrical coordinates is

$$\frac{1}{|\boldsymbol{x}-\boldsymbol{x}'|}=\frac{1}{\pi\sqrt{RR'}}\sum_{m=-\infty}^{\infty}e^{im(\phi-\phi')}Q_{m-1/2}(\chi)\,,$$

where $\chi\equiv[R^2+R'^2+(z-z')^2]/(2RR')$, and $Q_{m-1/2}$ is the half-integer degree Legendre function of the second kind. This expression is significantly more compact and easier to evaluate numerically than the more familiar cylindrical Green's function expression, which involves infinite integrals over products of Bessel functions and exponentials. It also contains far fewer terms in its series expansion—and is therefore more amenable to accurate evaluation—than does the familiar expression for $|\boldsymbol{x}-\boldsymbol{x}'|^{-1}$ that is given in terms of spherical harmonics. This compact Green's function expression is well suited for the solution of potential problems in a wide variety of astrophysical contexts because it adapts readily to extremely flattened (or extremely elongated), isolated mass distributions.

Subject headings: galaxies: formation — galaxies: structure — methods: analytical — stars: formation

1. INTRODUCTION

A great many astrophysical problems require the determination of a gravitational field. The field, for the most part, can be adequately described by Newtonian gravity and often can be derived from a potential function. From a mathematical viewpoint, there are two methods for obtaining the potential: by solving a partial differential equation, i.e., Poisson's equation, or by solving an integral equation, i.e., employing the Green's function method (Jackson 1975). As Arfken (1985) has explained, boundary conditions are directly built into the integral equation rather than being imposed at the final stage of the solution of a partial differential equation. Also, mathematical problems such as existence and uniqueness can be easier to handle when cast in integral form. On the other hand, solving differential equations is often more tractable than solving integral equations, particularly when dealing with multidimensional problems.

In building realistic models of steady state galaxies, a considerable amount of effort has been devoted in recent years toward identifying analytically prescribable potential-density pairs. In some cases a reasonable three-dimensional density distribution can be represented by a sum over a finite set of "basis density functions" in which case Poisson's equation can be solved using the corresponding basis sets of the potential-density pairs (Earn 1996; Robijn & Earn 1996). Some useful steady state models also can be constructed by superposing other special density (or surface-density) distributions with known potentials, such as those derivable from Stäckel potentials (de Zeeuw 1985; Evans & de Zeeuw 1992).

When following the time-evolutionary behavior of models whose structures are changing on a dynamical timescale, however, one must develop an efficient technique for solving Poisson's equation that works for arbitrary mass distributions. Furthermore, simulations of time-evolving systems often are carried out on grids that cover a finite (rather than an infinite) region of space, in which case one must also determine the potential on the boundary of that region. In practice, then, in many astrophysical studies a Green's function method is used to find the potential only on a boundary outside of a mass distribution, then a technique is developed to solve Poisson's equation to obtain the interior solution. A standard technique for calculating the boundary potential has been to expand the Green's function in spherical coordinates, resulting in what is often referred to as a "multipole method" (Black & Bodenheimer 1975; Norman & Wilson 1978; Barnes & Hut 1986; see also § 2.1, below) in which the potential is grouped into an infinite sum over a basis set of spherical harmonics described by two quantum numbers—one meridional, l, and the other azimuthal, m.

Because very flattened mass distributions are poorly described in a spherical coordinate system, we have examined whether it might be advantageous in our numerical simulations to cast the Green's function in a cylindrical coordinate system. The "familiar" expression for the cylindrical Green's function expansion can be found in variety of references (see Morse & Feshbach 1953; Jackson 1975; Arfken 1985). It is expressible in terms of an infinite sum over the azimuthal quantum number m and an infinite integral over products of Bessel functions of various orders multiplied by an exponential function (see eq. [13], below). We note a previous attempt by Villumsen (1985) to solve the potential problem in this manner; he presents a technique in which each infinite integral over products of Bessel functions is evaluated numerically using a Gauss-Legendre integrator. In that paper Villumsen states, "Cylindrical coordinates are a more natural coordinate system for disk systems." He then emphasizes the obvious problem that, because of the infinite integrals involved, a calculation of the potential via this straightforward application of the familiar cylindrical Green's function expansion is numerically much more difficult than a calculation of the potential using a spherical Green's function expansion.

In § 2.2 of this paper, we derive an extraordinarily compact expression for the Green's function in cylindrical

coordinates. Our expression (see eq. [15], below) completely removes the need for a numerical evaluation of the infinite integrals involved since we have found an analytical expression for the integral in terms of half-integer degree Legendre functions of the second kind. As we discuss in subsequent sections of this paper, our technique should prove to be a particularly powerful tool for studying self-gravitating systems that conform well to a cylindrical coordinate mesh, such as highly flattened (disk systems) or highly elongated (jet or bipolar flow) mass distributions.

As far as we have been able to ascertain, this result has not been previously derived. At the very least, based on published research over the past 30 years, the result appears to be unfamiliar to the astrophysics community.

2. A COMPARISON OF POTENTIAL EVALUATING TECHNIQUES

In general, the integral solution to the potential problem may be written in terms of the Green's function $\mathcal{G}(\boldsymbol{x}, \boldsymbol{x}')$ as follows (see eq. [1.42] of Jackson 1975):

$$\Phi(\boldsymbol{x}) = -G\int_V \rho(\boldsymbol{x}')\mathcal{G}(\boldsymbol{x}, \boldsymbol{x}')\,d^3x' + \frac{G}{4\pi}\oint_S \left[\Phi(\boldsymbol{x}')\frac{\partial \mathcal{G}(\boldsymbol{x}, \boldsymbol{x}')}{\partial n'} - \mathcal{G}(\boldsymbol{x}, \boldsymbol{x}')\frac{\partial \Phi}{\partial n'}\right] da' , \quad (1)$$

where Φ is the potential, G is the gravitational constant, ρ is the mass density, $\boldsymbol{x}$ denotes the position vector from the origin to the point at which the potential is being evaluated, $\boldsymbol{x}'$ denotes the position vector over which the mass integration is performed, V is the volume over which $\boldsymbol{x}'$ is integrated, and S is the bounding surface of V. For the case of no bounding surfaces—as in most astrophysical systems—the surface integral in equation (1) vanishes because of the requirement that both Φ and the derivative of Φ normal to the surface $\partial\Phi/\partial n'$ vanish at infinity. In this case the Green's function reduces to

$$\mathcal{G}(\boldsymbol{x}, \boldsymbol{x}') = \frac{1}{|\boldsymbol{x} - \boldsymbol{x}'|} . \quad (2)$$

These requirements therefore reduce equation (1) to the more often quoted integral expression for the gravitational potential, namely

$$\Phi(\boldsymbol{x}) = -G\int_V \rho(\boldsymbol{x}')\mathcal{G}(\boldsymbol{x}, \boldsymbol{x}')\,d^3x' = -G\int_V \frac{\rho(\boldsymbol{x}')}{|\boldsymbol{x} - \boldsymbol{x}'|}\,d^3x' . \quad (3)$$

2.1. *Multipole Method Using Spherical Harmonics*

In spherical coordinates, the expansion of the Green's function is (see eq. [3.70] of Jackson 1975)

$$\frac{1}{|\boldsymbol{x} - \boldsymbol{x}'|} = 4\pi\sum_{l=0}^{\infty}\sum_{m=-l}^{l}\frac{1}{2l+1}\frac{r_<^l}{r_>^{l+1}}Y_{lm}^*(\theta', \phi')Y_{lm}(\theta, \phi) , \quad (4)$$

where r represents the radial distance from the origin, θ is the polar angle, ϕ is the azimuthal angle, and Y_{lm} is the spherical harmonic function (see eq. [3.53] of Jackson 1975). If we insert equation (4) into equation (3), we obtain an expression for the potential at an exterior point ($r > r'$),

$$\Phi_{\rm ext}(\boldsymbol{x}) = \sum_{l=0}^{\infty}\sum_{m=-l}^{l}\frac{4\pi}{2l+1}\frac{Y_{lm}(\theta, \phi)}{r^{l+1}}q_{lm}^< , \quad (5)$$

where the coefficients

$$q_{lm}^< \equiv \int_V Y_{lm}^*(\theta', \phi')r'^l\rho(\boldsymbol{x}')\,d^3x' , \quad (6)$$

are called "multipole moments." In the case of an axisymmetric configuration, only the $m = 0$ terms in expression (4) survive, reducing it to

$$\left.\frac{1}{|\boldsymbol{x} - \boldsymbol{x}'|}\right|_{m=0} = \sum_{l=0}^{\infty}\frac{r_<^l}{r_>^{l+1}}P_l(\cos\theta')P_l(\cos\theta) . \quad (7)$$

The corresponding expression for the axisymmetric potential is therefore given by

$$\left.\Phi_{\rm ext}(r, \theta)\right|_{m=0} = -G\sum_{l=0}^{\infty}P_l(\cos\theta)r^{-(l+1)}M_l , \quad (8)$$

where now the axisymmetric multipole moments

$$M_l \equiv \int_V \rho(r', \theta')r'^l P_l(\cos\theta')\,d^3x' . \quad (9)$$

Expressions (5) or (8) for the gravitational potential have been adopted by many groups when developing numerical techniques to follow self-gravitating fluid flows on spherical or cylindrical coordinate meshes (Black & Bodenheimer 1975; Norman & Wilson 1978; Boss 1980; Tohline 1980; Stone & Norman 1992; Boss & Myhill 1995; Müller & Steinmetz 1995; Yorke & Kaisig 1995). As mentioned earlier, usually this multipole technique has been used to determine the potential everywhere along the bounding surface of the computational grid, then a separate technique has been developed to solve the Poisson equation in order to obtain the gravitational potential throughout the volume of the grid. However, when utilizing this multipole method, an exact determination of Φ for a discrete mass distribution is not possible because of the required infinite sum over the quantum number l. Instead, a decision must be made regarding when the series should be truncated in order to achieve a desired degree of accuracy for a given $\rho(\boldsymbol{x}')$ distribution. For example, referring to an expression for the axisymmetric potential analogous to our equation (8), Stone & Norman (1992) state that, "as implemented in ZEUS-2D, we continue to add higher moments until Φ_B has converged to one part in 10^3, up to a maximum of 100 terms."

One must also be sure that every location on the boundary of the computational grid $\boldsymbol{x}_B$ at which the exterior potential is being evaluated is at a radial location r_B that is greater than all interior grid locations at which matter resides. Otherwise $\Phi(\boldsymbol{x}_B)$ must be evaluated in two parts, namely,

$$\Phi(\boldsymbol{x}_B) = \Phi_{\rm ext}(\boldsymbol{x}_B) + \Phi_{\rm int}(\boldsymbol{x}_B) , \quad (10)$$

where $\Phi_{\rm int}(\boldsymbol{x}_B)$ must be determined through a separate integration over the mass that lies at radial locations greater than r_B. Specifically, the potential at an interior point ($r < r'$),

$$\Phi_{\rm int}(\boldsymbol{x}) = \sum_{l=0}^{\infty}\sum_{m=-l}^{l}\frac{4\pi}{2l+1}r^l Y_{lm}(\theta, \phi)q_{lm}^> , \quad (11)$$

where the coefficients

$$q_{lm}^> = \int_V \frac{Y_{lm}^*(\theta', \phi')}{r'^{l+1}}\rho(\boldsymbol{x}')\,d^3x' . \quad (12)$$

As we illustrate more fully in § 3.2, below, unless the boundary of a cylindrical grid is carefully designed so that it lies entirely outside the interior mass distribution (usually this means placing the grid boundary far away from the surface of the mass distribution), it will become necessary to calculate a separate set of "interior" and "exterior" moments of the mass distribution for the majority of boundary locations. This requirement will make the multipole method very computationally demanding, unless accuracy is sacrificed through a reduction in the number of terms that are included in the l summation.

2.2. *A Compact Cylindrical Green's Function Method*

2.2.1. *General Expressions*

In terms of the cylindrical coordinates (R, ϕ, z) the Green's function may be written as (e.g., problem [3.14] of Jackson 1975)

$$\frac{1}{|\boldsymbol{x}-\boldsymbol{x}'|}=\sum_{m=-\infty}^{\infty} e^{im(\phi-\phi')}\int_0^{\infty} dk\, J_m(kR)J_m(kR')e^{-k(z_>-z_<)}\,, \tag{13}$$

where J_m is an order m Bessel function of the first kind. Especially when faced with the problem of determining the gravitational potential on a cylindrical coordinate mesh, it would seem that this is a more appropriate expression to use for the Green's function than equation (4). As we discussed in § 1, however, devising an efficient numerical technique by which to accurately evaluate the infinite integral over products of Bessel functions has proven to be a difficult task.

Using equation (13.22.2) in Watson (1944), we recently have realized that

$$\int_0^{\infty} e^{-at}J_m(bt)J_m(ct)\,dt=\frac{1}{\pi\sqrt{bc}}\,Q_{m-1/2}\!\left(\frac{a^2+b^2+c^2}{2bc}\right), \tag{14}$$

where $Q_{m-1/2}$ is the half-integer degree Legendre function of the second kind. Hence, it becomes possible to rewrite equation (13) as

$$\frac{1}{|\boldsymbol{x}-\boldsymbol{x}'|}=\frac{1}{\pi\sqrt{RR'}}\sum_{m=-\infty}^{\infty} e^{im(\phi-\phi')}Q_{m-1/2}(\chi)\,, \tag{15}$$

with

$$\chi\equiv\frac{R^2+R'^2+(z-z')^2}{2RR'}\,. \tag{16}$$

We note that this same result for the Green's function can be obtained by combining equation (3.148) in Jackson (1975) with equation (6.672.4) in Gradshteyn & Ryzhik (1994). Although relationship (14) and, hence, the ability to derive (15) from (13), has been known for some time, apparently the astrophysics community has not been aware that the cylindrical Green's function can be expressed in this extraordinarily compact form. As we shall demonstrate, highly accurate and efficient means of evaluating $\Phi(\boldsymbol{x})$ can be developed from expression (15).

Realizing that $Q_{-1/2+m}(\chi)=Q_{-1/2-m}(\chi)$ (cf. eq. [8.736.7] in Gradshteyn & Ryzhik 1994), and that $e^{i\theta}+e^{-i\theta}=2\cos\theta$, we can express equation (15) in terms of all $m\geq 0$ as

$$\frac{1}{|\boldsymbol{x}-\boldsymbol{x}'|}=\frac{1}{\pi\sqrt{RR'}}\sum_{m=0}^{\infty}\epsilon_m\cos\left[m(\phi-\phi')\right]Q_{m-1/2}(\chi)\,, \tag{17}$$

where ϵ_m is the Neumann factor (Morse & Feshbach 1953), that is, $\epsilon_0=1$ and $\epsilon_m=2$ for $m\geq 1$. Now we substitute equation (17) into equation (3), obtaining

$$\Phi(\boldsymbol{x})=-\frac{G}{\pi\sqrt{R}}\int_V d^3x'\frac{\rho(\boldsymbol{x}')}{\sqrt{R'}}\sum_{m=0}^{\infty}\epsilon_m \times\cos\left[m(\phi-\phi')\right]Q_{m-1/2}(\chi)\,, \tag{18}$$

which may also be rewritten as

$$\begin{aligned}\Phi(\boldsymbol{x})=&-\frac{G}{\pi\sqrt{R}}\int_V d^3x'\frac{\rho(\boldsymbol{x}')}{\sqrt{R'}}\,Q_{-1/2}(\chi)\\&-\frac{2G}{\pi\sqrt{R}}\sum_{m=1}^{\infty}\cos(m\phi)\int_V d^3x'\frac{\rho(\boldsymbol{x}')}{\sqrt{R'}}\cos(m\phi')Q_{m-1/2}(\chi)\\&-\frac{2G}{\pi\sqrt{R}}\sum_{m=1}^{\infty}\sin(m\phi)\int_V d^3x'\frac{\rho(\boldsymbol{x}')}{\sqrt{R'}}\sin(m\phi')Q_{m-1/2}(\chi)\,.\end{aligned} \tag{19}$$

Finally, an azimuthal discrete Fourier transform of this last expression yields the following elegant representation of the gravitational potential in Fourier space:

$$\Phi_m^{1,2}(R,z)=-\frac{G\epsilon_m}{\sqrt{R}}\int_{\Sigma}d\sigma'\sqrt{R'}\rho_m^{1,2}(R',z')Q_{m-1/2}(\chi)\,, \tag{20}$$

where Σ refers to the area over which the meridional integration is to be carried, $d\sigma'=dR'\,dz'$, and the Fourier components of Φ and ρ are defined such that

$$\begin{aligned}\begin{Bmatrix}\Phi\\ \rho\end{Bmatrix}(\boldsymbol{x})=&\sum_{m=0}^{\infty}\cos(m\phi)\begin{Bmatrix}\Phi_m^1\\ \rho_m^1\end{Bmatrix}(R,z)\\&+\sum_{m=0}^{\infty}\sin(m\phi)\begin{Bmatrix}\Phi_m^2\\ \rho_m^2\end{Bmatrix}(R,z)\,.\end{aligned} \tag{21}$$

(Note that $\Phi_0^2=\rho_0^2=0$.)

2.2.2. *Functional Forms of $Q_{m-1/2}$*

Useful expressions for $Q_{-1/2}(\chi)$ and $Q_{1/2}(\chi)$ may be obtained from equations (8.13.3) and (8.13.7), respectively, of Abramowitz & Stegun (1965), namely,

$$Q_{-1/2}(\chi)=\mu K(\mu) \tag{22}$$

and

$$Q_{1/2}(\chi)=\chi\mu K(\mu)-(1+\chi)\mu E(\mu)\,, \tag{23}$$

where K represents the complete elliptic integral of the first kind, E is the complete elliptic integral of the second kind, and

$$\mu\equiv\sqrt{\frac{2}{1+\chi}}=\sqrt{\frac{4RR'}{(R+R')^2+(z-z')^2}}\,. \tag{24}$$

One can then obtain the higher degree half-integer Legendre functions of the second kind using the recurrence relation (e.g., eq. [8.5.3] in Abramowitz & Stegun 1965)

$$Q_{m-1/2}(\chi)=4\,\frac{m-1}{2m-1}\,\chi Q_{m-3/2}(\chi)-\frac{2m-3}{2m-1}\,Q_{m-5/2}(\chi)\,. \tag{25}$$

For example, substituting equations (22) and (23) into equation (25) gives the following useful expression for $Q_{3/2}(\chi)$:

$$Q_{3/2}(\chi) = (\tfrac{4}{3}\chi^2 - \tfrac{1}{3})\mu K(\mu) - \tfrac{4}{3}\chi(1+\chi)\mu E(\mu)\,. \quad (26)$$

According to Table XIII in Tables of Associated Legendre Functions (US. NBS. Comput. Lab. 1945), we may also express $Q_{m-1/2}(\chi)$ in terms of Gauss's hypergeometric function as follows:

$$Q_{m-1/2}(\chi) = \frac{\sqrt{\pi}\Gamma(m+1/2)}{2^{m+1/2}\Gamma(m+1)\chi^{m+1/2}} \times {}_2F_1\left(\frac{2m+3}{4}, \frac{2m+1}{4}; m+1; \frac{1}{\chi^2}\right), \quad (27)$$

where the specific hypergeometric function

$${}_2F_1(a, b; c; y) = \frac{\Gamma(c)}{\Gamma(a)\Gamma(b)} \sum_{n=0}^{\infty} \frac{\Gamma(a+n)\Gamma(b+n)y^n}{\Gamma(c+n)n!}, \quad (28)$$

and Γ is the Gamma function (see eq. [6.1.1] of Abramowitz & Stegun 1965). Inserting equation (28) into equation (27), we derive the following expression:

$$Q_{m-1/2}(\chi) = \frac{\Gamma(m+1/2)\sqrt{\pi}}{\Gamma[(2m+3)/4]\Gamma[(2m+1)/4](2\chi)^{m+1/2}} \times \sum_{n=0}^{\infty} \frac{\Gamma[(2m+4n+3)/4]\Gamma[(2m+4n+1)/4]}{\Gamma(m+1+n)\Gamma(1+n)\chi^{2n}}\,. \quad (29)$$

It is well known (see Abramowitz & Stegun 1965) that Legendre functions of the second kind are singular when their arguments are unity. Evaluating the limit of $Q_{m-1/2}(\chi)$ in equation (29) for large values of χ gives the asymptotic behavior of $Q_{m-1/2}(\chi)$ (with only the $n = 0$ term in the sum surviving):

$$\lim_{\chi\to\infty} Q_{m-1/2}(\chi) = \frac{\Gamma(m+1/2)\sqrt{\pi}}{\Gamma(m+1)(2\chi)^{m+1/2}}\,, \quad (30)$$

which decays as $1/\chi^{m+1/2}$.

3. SUBSTANTIATIONS

In this section, we verify the correctness and highlight the utility of the compact cylindrical Green's function (CCGF) representation by comparing expressions for the Newtonian potential derived from it with previously known results. We show that the familiar expression for the potential of an infinitesimally thin, axisymmetric disk in terms of complete elliptic integrals can be readily derived from equation (19). We also show how this expression can be generalized to axisymmetric systems of arbitrary vertical thickness and how an analogous expression for any other isolated azimuthal Fourier mode can now be readily derived. In the context of nonaxisymmetric fields, we show how Kalnajs' reduced potential for an infinitesimally thin, nonaxisymmetric disk can be readily derived via our CCGF expression, and we draw on one more specific problem from magnetostatics to demonstrate how the CCGF reproduces the exact analytical expression for a potential problem where the solution can be expressed entirely in terms of the $m = 1$ ($Q_{1/2}$) nonaxisymmetric term.

Finally, for several "geometrically thick" configurations of uniform density, we provide numerical comparisons between $\Phi(\boldsymbol{x}_B)$ as derived from the CCGF method and as determined from (1) the traditional multipole method and (2) analytical prescriptions, where available. In § 3.3 we comment on the computational advantages and disadvantages of the CCGF method when the objective is to determine values of the gravitational potential outside, but in close proximity to, flattened or elongated mass distributions. Generally speaking, for a given computational grid resolution we find that the CCGF method provides more accurate values of $\Phi(\boldsymbol{x}_B)$ in equal or less computational time than using the multipole method, but in certain situations the CCGF method can be quite demanding in terms of memory storage requirements.

3.1. *Analytical Verifications and Propositions*

3.1.1. *Axisymmetric Systems with Vertical Extent*

For an axisymmetric mass distribution, equation (19) reduces to the form

$$\Phi_0(R, z) = -\frac{2G}{\sqrt{R}}\, q_0\,, \quad (31)$$

with

$$q_0 \equiv \int_\Sigma d\sigma' \sqrt{R'}\, \rho(R', z') Q_{-1/2}(\chi) \quad (32a)$$

$$= \int_\Sigma d\sigma' \sqrt{R'}\, \rho(R', z') \mu K(\mu)\,, \quad (32b)$$

where χ and μ have been defined by equations (16) and (24), respectively. As we shall illustrate in § 3.2, this expression can be used effectively to compute the potentials outside of oblate spheroids, prolate spheroids, tori, or thick disks with arbitrarily complex $\rho(R, z)$ distributions.

It is important to note that equation (31) provides an expression for the gravitational potential of an axisymmetric mass distribution that contains a single term and a single moment of the mass distribution q_0. In contrast to this, the corresponding expression for the potential in spherical coordinates [eq. (8)] requires a summation over an infinite number of terms, each containing a different moment of the mass distribution. Hence, equation (31) provides an expression for the potential that is easier to evaluate and guaranteed to be more accurate (for a given computational grid resolution) than equation (8). We strongly recommend its adoption in numerical algorithms that are designed to study self-gravitating, axisymmetric fluid flows.

3.1.2. *Infinitesimally Thin Axisymmetric Systems*

In the case of an infinitesimally thin axisymmetric disk located in the plane $z' = 0$, the density distribution can be written as

$$\rho(R', z') = \Sigma(R')\,\delta(z')\,, \quad (33)$$

where $\Sigma(R')$ is the surface density of the disk and $\delta(z')$ is a Dirac delta function. Inserting this expression for $\rho(R', z')$ into equation (32b) and integrating over z', we obtain the following exact expression for the gravitational potential of any infinitesimally thin, axisymmetric disk:

$$\Phi_{0,\mathrm{disk}}(R, z) = -\frac{2G}{\sqrt{R}} \int_0^\infty dR' \sqrt{R'}\, \Sigma(R') \mu_d K(\mu_d)\,, \quad (34)$$

where

$$\mu_d \equiv \sqrt{\frac{4RR'}{(R+R')^2+z^2}}\,. \tag{35}$$

This equation exactly matches the expression for the potential of an infinitesimally thin, axisymmetric galaxy disk given, for example, by equation (2-142a) of Binney & Tremaine (1987). It is now clear through equations (31) and (32) that this familiar expression can be generalized to axisymmetric configurations with arbitrary vertical extent.

3.1.3. *Nonaxisymmetric Systems and Kalnajs Logarithmic Spirals*

Here we demonstrate that the expression for the reduced potential of an infinitesimally thin, nonaxisymmetric disk that has been developed by Kalnajs (1971; see also, for example, § 2.4b of Binney & Tremaine 1987) can be readily derived from our CCGF. Guided by a key functional relationship found in Morse & Feshbach (1953), we show through a brief derivation in Appendix A (see specifically eq. [A5]) that

$$\sum_{m=0}^{\infty} \epsilon_m \cos(m\phi) Q_{m-1/2}(\cosh\mu) = \frac{\pi}{\sqrt{2}} \frac{1}{\sqrt{\cosh\mu - \cos\phi}}\,. \tag{36}$$

Hence, expression (17) for the Green's function can be rewritten as

$$\frac{1}{|\boldsymbol{x}-\boldsymbol{x}'|} = \frac{1}{\sqrt{2RR'}} \frac{1}{\sqrt{\cosh\xi - \cos(\phi-\phi')}}\,, \tag{37}$$

where

$$\xi \equiv \cosh^{-1}(\chi) = \ln\left(\chi + \sqrt{\chi^2-1}\right). \tag{38}$$

Combining this expression with equation (3), we may therefore also conclude that the "reduced potential,"

$$V(\boldsymbol{x}) \equiv \sqrt{R}\Phi(\boldsymbol{x}) = -G\int_V \frac{1}{\sqrt{R'}} \frac{\rho(\boldsymbol{x}')}{\sqrt{2[\cosh\xi - \cos(\phi-\phi')]}}\, d^3\boldsymbol{x}' \tag{39}$$

$$= -G\int_0^{\infty} \frac{dR'}{R'} \int_0^{2\pi} d\phi' \int_{-\infty}^{\infty} dz' \times \left\{ \frac{R'^{3/2}\rho(\boldsymbol{x}')}{\sqrt{2[\cosh\xi - \cos(\phi-\phi')]}} \right\}. \tag{40}$$

Now, if we consider an infinitesimally thin disk located in the plane $z' = 0$, the density distribution can be written as

$$\rho(\boldsymbol{x}') = \delta(z')\Sigma(R', \phi')\,, \tag{41}$$

where $\Sigma(R', \phi')$ represents an arbitrary nonaxisymmetric surface density distribution, and the integral over z' in equation (40) can be completed, giving

$$V(R,\phi) = -G\int_0^{\infty} \frac{dR'}{R'} \int_0^{2\pi} d\phi' \left[R'^{3/2}\Sigma(R', \phi')\right] \times \frac{1}{\sqrt{2}} \frac{1}{\sqrt{\cosh\left[\ln(R/R')\right] - \cos(\phi-\phi')}}\,. \tag{42}$$

If, finally, we define a reduced surface density,

$$S(R,\phi) \equiv R^{3/2}\Sigma(R,\phi)\,, \tag{43}$$

and adopt in place of R the independent variable

$$u \equiv \ln R\,, \tag{44}$$

we obtain

$$V(u,\phi) = -G\int_{-\infty}^{\infty} du' \int_0^{2\pi} d\phi'\, S(u', \phi')\mathcal{K}_{2D}(u-u', \phi-\phi')\,, \tag{45}$$

where

$$\mathcal{K}_{2D}(u-u', \phi-\phi') \equiv \frac{1}{\sqrt{2[\cosh(u-u') - \cos(\phi-\phi')]}}\,. \tag{46}$$

Equation (45) is the expression Kalnajs (1971) has provided for the reduced potential of an infinitesimally thin, nonaxisymmetric disk. It is via this expression that Kalnajs has realized the utility of viewing nonaxisymmetric surface density distributions in terms of their various "logarithmic spiral" components.

Our expression (40) may now be viewed as a generalization of Kalnajs' reduced potential that applies to nonaxisymmetric structures of arbitrary vertical thickness, the key difference being that, in our more generalized expression for the reduced potential, the function $\mathcal{K}_{2D}(u-u', \phi-\phi')$ must be replaced by the function

$$\mathcal{K}_{3D}(\chi, \phi-\phi') \equiv \frac{1}{\sqrt{2[\chi - \cos(\phi-\phi')]}}\,, \tag{47}$$

where, as defined in equation (16), χ itself is a function that involves a nontrivial coupling between the coordinate variables R, R', z and z'. Although, as indicated by expression (38), it is possible to rewrite $\cosh^{-1}(\chi)$ in terms of a logarithmic function and, in so doing, transform equation (47) into a form that more closely resembles Kalnajs' function $\mathcal{K}_{2D}$, the nontrivial coupling between coordinate variables within χ makes such a formulation less compelling in the full three-dimensional problem.

3.1.4. *The $m = 1$ Mode and the Magnetic Field of a Current Loop*

A derivation of the magnetic field of a time-independent circular current loop of radius a, and current I has been provided in a multitude of classical electromagnetism textbooks (e.g., Landau & Lifshitz 1960; Jackson 1975). Here we demonstrate that this classic problem can be readily solved via the CCGF. In a magnetostatics problem we may calculate the magnetic field from a vector potential, $\boldsymbol{A}(\boldsymbol{x})$, as follows:

$$\boldsymbol{B}(\boldsymbol{x}) = \nabla \times \boldsymbol{A}(\boldsymbol{x})\,. \tag{48}$$

Then in the Coulomb gauge the vector potential satisfies the following vector Poisson equation:

$$\nabla^2 \boldsymbol{A}(\boldsymbol{x}) = -\frac{4\pi}{c}\boldsymbol{J}(\boldsymbol{x})\,, \tag{49}$$

where $\boldsymbol{J}(\boldsymbol{x})$ is the current density and c is the speed of light. The integral solution of this vector Poisson equation produces the magnetic analogue of equation (3), namely,

$$\boldsymbol{A}(\boldsymbol{x}) = \frac{1}{c}\int_V \frac{\boldsymbol{J}(\boldsymbol{x}')}{|\boldsymbol{x}-\boldsymbol{x}'|}\, d^3x'\,. \tag{50}$$

In the case of a circular current loop located in the equatorial plane, $z' = 0$, the current density has only a ϕ component, which is

$$\boldsymbol{J}(\boldsymbol{x}) = \hat{\phi} J_\phi \,, \tag{51}$$

where

$$J_\phi(\boldsymbol{x}') = I \cos(\phi')\, \delta(z')\, \delta(R' - a) \,. \tag{52}$$

Since the final solution must be invariant under rotation, we choose our observing point to be at $\phi = 0$. Substituting equations (51) and (17) into equation (50), we obtain the following expression for the ϕ component of the vector potential:

$$A_\phi = \frac{I}{\pi c} \sqrt{\frac{a}{R}} \int_0^{2\pi} d\phi' \cos(\phi') \sum_{m=0}^{\infty} \epsilon_m \cos(m\phi') Q_{m-1/2}(\chi_l) \,, \tag{53}$$

where

$$\chi_l \equiv \frac{R^2 + a^2 + z^2}{2Ra} \,. \tag{54}$$

The only term in the summation that contributes is the $m = 1$ term, so equation (53) becomes

$$A_\phi = \frac{2I}{\pi c} \sqrt{\frac{a}{R}}\, Q_{1/2}(\chi_l) \int_0^{2\pi} \cos^2(\phi')\, d\phi' = \frac{2I}{c} \sqrt{\frac{a}{R}}\, Q_{1/2}(\chi_l) \,, \tag{55}$$

which, via equation (23), can be rewritten as

$$A_\phi = \frac{4Ia}{c\sqrt{(R+a)^2 + z^2}} \left[\frac{(2 - \mu_l^2) K(\mu_l) - 2E(\mu_l)}{\mu_l^2} \right] . \tag{56}$$

This identically reproduces the previously known result for the vector potential of a current loop (e.g., eq. [5.37] in Jackson 1975).

3.1.5. *The $m = 2$ and Other Isolated Fourier Modes*

In § 3.1.1, we used the CCGF method to derive a general expression that describes the $m = 0$ (axisymmetric) Fourier mode contribution to the gravitational potential for any mass distribution. Here we illustrate how similarly simple expressions for any other isolated azimuthal mode of a self-gravitating system can be derived via equation (20). For an $m = 2$ distortion, for example, the two relevant Fourier components of the potential are

$$\Phi_2^{1,2}(R, z) = -\frac{2G}{\sqrt{R}} \int_\Sigma d\sigma' \sqrt{R'} \rho_2^{1,2}(R', z') Q_{3/2}(\chi) \,. \tag{57}$$

Utilizing equation (26), which was derived in § 2.2.2 via the recurrence relation for half-integer degree Legendre functions of the second kind, we are able to rewrite this expression for $\Phi_2^{1,2}(R, z)$ in terms of more familiar elliptic integrals as follows:

$$\Phi_2^{1,2}(R, z) = -\frac{2G}{3\sqrt{R}} \int_\Sigma d\sigma' \sqrt{R'} \rho_2^{1,2}(R', z') \times \mu[(4\chi^2 - 1)K(\mu) - 4\chi(1 + \chi)E(\mu)] \,. \tag{58}$$

Furthermore, in the case of an infinitesimally thin disk the Fourier components of the density can be written as

$$\rho_2^{1,2}(R', z') = \Sigma_2^{1,2}(R')\, \delta(z') \,, \tag{59}$$

and we obtain the following exact expression for the $m = 2$ Fourier components of the potential of any infinitesimally thin, self-gravitating disk:

$$\Phi_{2,\mathrm{disk}}^{1,2}(R, z) = -\frac{2G}{3\sqrt{R}} \int_0^\infty dR' \sqrt{R'}\, \Sigma_2^{1,2}(R') \mu_d \times [(4\chi_d^2 - 1)K(\mu_d) - 4\chi_d(1 + \chi_d)E(\mu_d)] \,, \tag{60}$$

where $\chi_d \equiv 2/\mu_d^2 - 1$. This compact analytical expression should prove useful in, for example, studies of $m = 2$ spiral-arm instabilities in self-gravitating galaxy or protostellar disks.

3.2. *Numerical Evaluations*

Here we perform a variety of numerical tests in which we have discretized selected mass-density distributions on a uniformly zoned cylindrical coordinate mesh. We have selected these models in order to elucidate the power that the CCGF method offers as a numerical technique for evaluating exterior potentials surrounding self-gravitating objects. Our comparison incorporates three methods for potential evaluation: (1) analytical potential-density expressions, as drawn from the works of other authors and detailed here in Appendix B; (2) the multipole method described in § 2.1; and (3) our CCGF method, as outlined in § 2.2. Where available, analytical solutions provide extremely useful verification of numerical methods for potential evaluation since any valid method should yield asymptotic convergence toward the analytical solution with increased grid resolution. Most of the models we have selected have known analytical solutions. In cases where the analytical solution does not exist, we simply compare the potentials obtained through the CCGF and multipole methods.

Table 1 lists the five models we have selected, and Table 2 summarizes the seven tests that we have conducted using these models. Each of the five selected models has a uniform density distribution that is enclosed within a surface of a

TABLE 1

MODELS

Model	Type of Object	Aspect Ratio	Equation Number
I.....	Oblate spheroid	5:1	B2
II.....	Oblate spheroid	20:1	B2
III.....	Prolate spheroid	20:1	B2
IV.....	Torus	20:1	...
V.....	Triaxial ellipsoid	20:10:1	B7

TABLE 2

TESTS

Test	Model	Grid Resolution
1	I	128 × 128
2	I	128 × 32
3	II	1024 × 64
4	III	32 × 512
5	IV	512 × 32
6[a].....	I	$J \times K$
7	V	512 × 32 × 256

[a] $J = 32i$, $K = 8i$, with $(1 < i < 25)$.

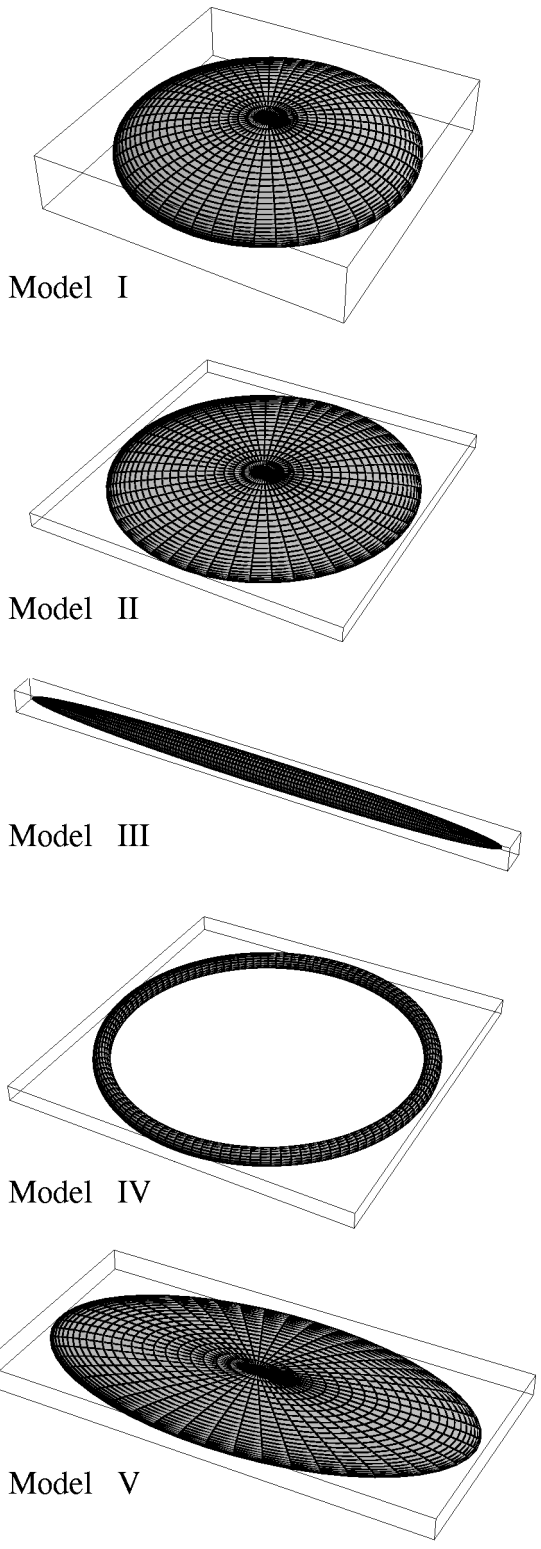

FIG. 1.—Three-dimensional wire-frame diagrams illustrating the geometry of the five uniform-density models for which the external gravitational potential has been calculated herein using the CCGF technique ($\Phi^{\mathcal{Q}}$) and compared with approximate solutions obtained via a standard multipole technique ($\Phi^{\mathcal{Y}}$) and (where available) exact analytical expressions ($\Phi^{\mathcal{A}}$). See Table 1 for details regarding each test model's selected aspect ratio.

well-defined geometry as described by the "type of object" column in Table 1. Figure 1 portrays the above described models through a three-dimensional isosurface visualization of each homogeneous object's boundary. The oblate, prolate, and toroidal objects are all axisymmetric. For the two oblate spheroids (models I and II), the aspect ratios listed in Table 1 define the size of the equatorial axis relative to the polar axis. For the prolate spheroid (model III), the 20:1 aspect ratio describes the size of the polar axis relative to the equatorial axis. For the torus (model IV), the aspect ratio describes the size of the major radius of the torus relative to its minor, cross-sectional radius. Finally, we also have chosen one nonaxisymmetric model, model V, which is a 20:10:1 triaxial homogeneous ellipsoid.

The column labeled "grid resolution" in Table 2 specifies the size of the computational grid or grids that was used in each test. For each axisymmetric model (tests 1–6), the stated resolution $J \times K$ refers to the number of radial (J) and vertical (K) zones used; for model V (test 7), the stated resolution $J \times K \times L$ includes the number of azimuthal (L) zones that were used as well. For each of the tests identified in Table 2, we have determined the fractional error of a given numerical solution for the potential Φ by measuring at every location along the top and side boundaries of our cylindrical grid the quantity

$$\epsilon \equiv \frac{\Phi - \Phi^*}{\Phi^*}\,, \tag{61}$$

where Φ^* is the "known" solution. Figures 2–7 present subsets of these error measurements in various ways. In presenting the results of these tests, the numerically derived potential Φ is either the Newtonian potential generated via the multipole method, $\Phi^{\mathcal{Y}}$, or via the CCGF method, $\Phi^{\mathcal{Q}}$. Where available, the known solution Φ^* is given by the analytical solution, $\Phi^{\mathcal{A}}$, as drawn from the relevant Appendix B expression and identified by the entry in the "equation number" column of Table 1. Otherwise we take Φ^* to be $\Phi^{\mathcal{Q}}$, since we recognize it as the more correct numerical solution for the discretized model. Note that in test 6, model I has been reexamined using 25 different grid resolutions. This has been done in order to ascertain how the determination of $\Phi^{\mathcal{Q}}$ relative to $\Phi^{\mathcal{A}}$ improves with grid resolution.

3.2.1. *Axisymmetric Models*

For the four axisymmetric models listed in Table 1, $\Phi^{\mathcal{Q}}$ has been determined via equation (31) and its associated moment of the mass distribution as defined by equation (32b). The thick-dashed curves in Figures 2, 3, and 4 represent the fractional error obtained by comparing $\Phi^{\mathcal{Q}}$ with $\Phi^{\mathcal{A}}$ for models I, II, and III, respectively. Since, as emphasized in § 3.1.1, equation (31) provides an expression for the gravitational potential that contains only one term, any error that arises in the determination of $\Phi^{\mathcal{Q}}$ relative to $\Phi^{\mathcal{A}}$ must be entirely attributed to the fact that, at any finite grid resolution, a numerical integration of equation (32b) cannot possibly give the precise analytical answer. It is important to appreciate that this "failing" has nothing to do with our ability to evaluate the special function $K(\mu)$ accurately. Instead, it stems from the fact that the models for which we have analytically known potentials have spheroidal surfaces, and it is impossible to represent such surfaces precisely within a cylindrical coordinate mesh. Indeed, even a straightforward volume integration over the density distribution will give a total mass that is different from the analytically "known" mass because a spheroidal object cannot be perfectly represented in a cylindrical mesh. We shall return to this issue when discussing test 6, below.

In contrast to this, errors in the determination of Φ^Y are dominated by the fact that, in any practical implementation of the multipole method, the summation over multipole moments must be truncated at some finite number of terms, l_{max}. Only in the limit $l_{max} \to \infty$ will the value of Φ^Y given by equation (8) for an axisymmetric mass distribution converge to the value of Φ^Q given by equation (31), for example. Because the contribution that each multipole moment makes to the potential drops off as $r^{-(l+1)}$, a reasonably small error can be realized with a reasonably small value of l_{max} if the boundary cells at which Φ^Y is to be evaluated are placed at locations r that are fairly far from the mass distribution. For each of the seven tests listed in Table 2, Φ^Y has been determined for six different even values of l_{max} in the range $0 \le l_{max} \le 10$ in an effort to illustrate how rapidly the determination of Φ^Y converges toward Φ^A and Φ^Q as more and more terms are included in the l summation. We illustrate results only for even values of l_{max} because all five models listed in Table 1 exhibit reflection symmetry through the equatorial plane and, by design, this symmetry forces all odd multipole moments to be identically zero. In each of Figures 2–5 and 7, dotted curves illustrate errors in the determinations of Φ^Y when $l_{max} = 0$; thin-dashed curves represent errors resulting from setting $l_{max} = 2$; and the dot-dashed curves show errors in Φ^Y resulting from the inclusion of even multipole moments through $l_{max} = 10$. The three solid curves generally lying between the thin-dashed curve and the dot-dashed curve in each figure represent, in sequence, errors in Φ^Y that result from setting $l_{max} =$ 4, 6, and 8.

Figure 2 illustrates results from tests 1 and 2 on model I (the 5:1 oblate spheroid). In both of these tests, our computational mesh had 128 radial grid zones of uniform radial (ΔR) and vertical ($\Delta z = \Delta R$) thickness, and the oblate spheroid was positioned such that its equatorial radius extended out to grid location 123. Tests 1 and 2 differed in only one respect, as indicated in Table 2: with a cylindrical computational mesh that had 4 times as many vertical zones, test 1 was designed to place the top boundary of the computational grid much farther from the surface of the oblate spheroid than in test 2. Because every point along the boundary of the grid in test 1 was at a radial location r_B greater than the equatorial radius of the model I spheroid, Φ^Y was evaluated using equations (5) and (6), with m set equal to zero, as in equations (8) and (9). However, in test 2 it was also necessary to include an evaluation of Φ_{int} (eq.

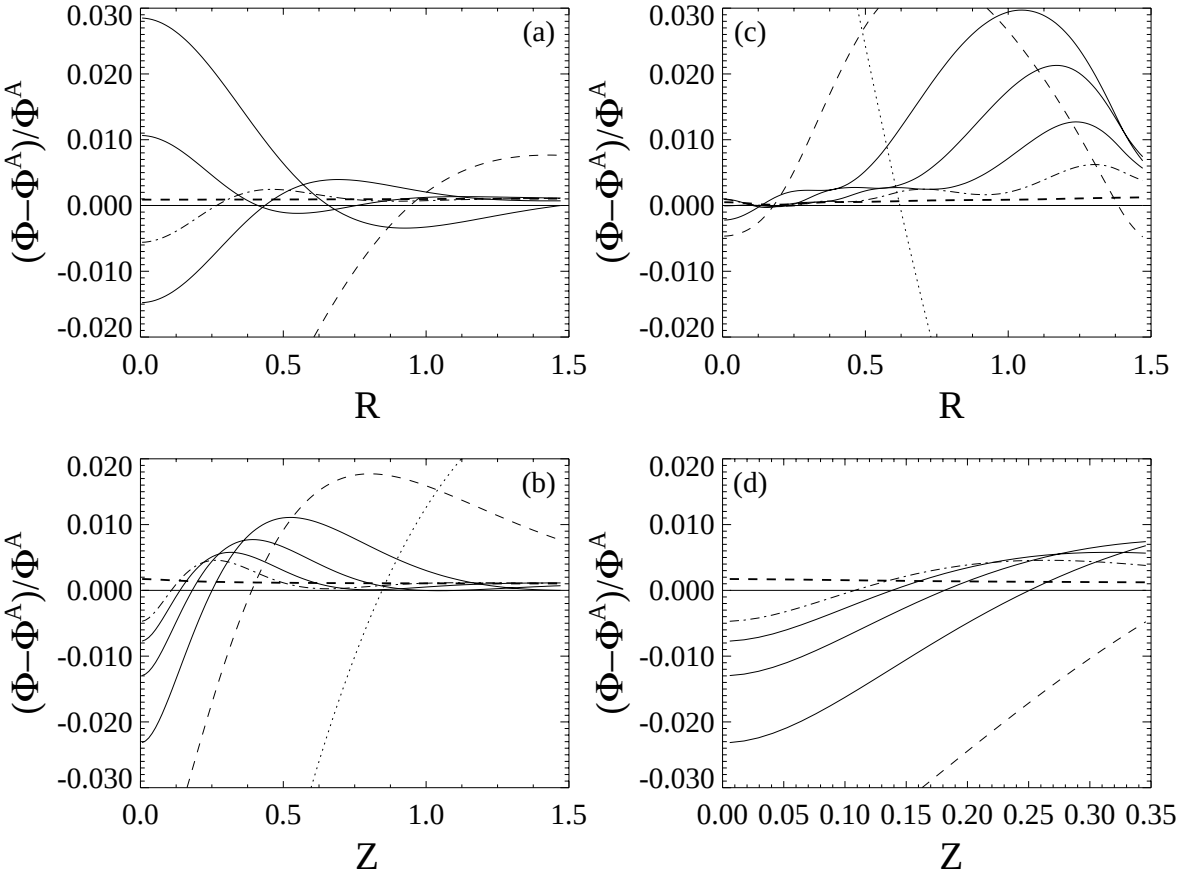

FIG. 2.—Model I (5:1 oblate spheroid). The fractional error in the numerically determined gravitational potential (calculated via two different Green's function techniques) relative to the analytically known potential Φ^A is shown here as a function of position R along the top and Z along the side boundaries of the selected cylindrical computational mesh, as defined in Table 2. (*a* and *b*) Results from test 1 in which the top boundary of a 128 × 128 computational mesh has been positioned at the same distance from the center of the grid as the side boundary. A thin, solid horizontal line has been drawn at zero for reference purposes. The thick dashed line running approximately horizontally across both frames shows the errors in the potential as determined via the CCGF technique, i.e., $(\Phi^Q - \Phi^A)/\Phi^A$. (See the discussion associated with test 6 for an explanation of why these curves are slightly offset from zero.) All other curves illustrate the errors in the potential as determined via the standard multipole technique i.e., $(\Phi^Y - \Phi^A)/\Phi^A$, as the limiting number of terms in the multipole expansion is increased successively by 2 from $l = 0$ (*dotted curves*) to $l = 2$ (*dashed curves*), etc., through $l = 10$ (*dot-dashed curves*). (*c* and *d*) Same type of information as displayed in (*a*) and (*b*), respectively, but for test 2, in which the top boundary of a 128 × 32 computational mesh has been placed a factor of 4 closer to the center of the grid, in a position that lies very close to the surface of the model I spheroid. Results from this test 2 also appear as the example marked "A" in Fig. 6.

[11]) and, hence, a separate evaluation of $q_{lm}^{>}$ and $q_{lm}^{<}$, for each zone along the top of the grid boundary. As a result (see the related discussion in § 3.3, below), the evaluation of $\Phi^{\mathcal{Y}}$ in test 2 was much more computationally demanding than in test 1. Errors in the determination of the potential along the top boundary of these two different cylindrical computational domains are shown in Figures 2*a* and 2*c*; corresponding errors along the side boundary are displayed in Figures 2*b* and 2*d*.

The results presented in Figure 2 highlight three key points that have been discussed in a more general context, above. First, in both tests $\Phi^{\mathcal{Q}}$ very nearly follows the analytically derived potential $\Phi^{\mathcal{A}}$ at all locations on the grid boundary. It is, however, everywhere offset from $\Phi^{\mathcal{A}}$ by a small amount. This small offset is due almost entirely to the effect mentioned above of being unable to properly represent a perfect spheroidal surface within a cylindrical coordinate grid. Second, as $l_{\max}$ is increased, the multipole method yields better and better results that converge toward the solution $\Phi^{\mathcal{Q}}$, but in no case is the typical error in $\Phi^{\mathcal{Y}}$ smaller than the typical error in $\Phi^{\mathcal{Q}}$. Third, for a given choice of $l_{\max}$, the typical error in $\Phi^{\mathcal{Y}}$ measured along the top of the cylindrical grid is smaller in test 1 (Fig. 2*a*) than it is in test 2 (Fig. 2*c*). This is because the top of the grid is farther from the surface of the mass distribution in test 1 than in test 2.

Figure 3 illustrates the results from test 3 on model II (the 20:1 oblate spheroid). This test is similar to test 2 in that the top boundary of the computational grid has been placed very close to the surface of the spheroid. In one quadrant of a meridional plane cutting through model II, Figure 3*a* illustrates precisely where the top and side cylindrical boundaries have been placed with respect to the surface of the spheroid. Test 3 differs from test 2, however, in that the spheroidal model for which the gravitational potential is being determined has a relatively extreme (20:1) axis ratio. In order to maintain a uniformly zoned computational grid, a correspondingly extreme radial to vertical (1024 × 64) grid resolution was adopted for test 3. In addition to displaying in Figure 3*c* the fractional errors that resulted from our determinations of $\Phi^{\mathcal{Y}}$ and $\Phi^{\mathcal{Q}}$ along the top boundary of the computational grid, we have shown in Figure 3*b* the functional variation of the boundary potentials from which the errors displayed in Figure 3*c* have been derived. This is a particularly severe test of the multipole moment method because the potential of extremely flattened mass distributions is not well represented by an expansion in terms of spherical harmonics. Notice, however, that the CCGF method has no difficulty evaluating the potential for this extremely flattened spheroid; in both Figures 3*b* and 3*c* the thick-dashed curve representing $\Phi^{\mathcal{Q}}$ is nearly indistinguishable from the thin solid line representing $\Phi^{\mathcal{A}}$.

In Figure 4 we show results from test 4 on model III, the 20:1 prolate spheroid. For this test, the model has been discretized on a 32 × 512 cylindrical grid. In this case, the primary challenge for both the multipole moment and CCGF methods is to accurately evaluate the potential along the side, rather than the top, of the computational grid. Figure 4*a* shows the fractional error as a function of z along the side of this highly elongated coordinate mesh, and Figure 4*b* shows the fractional error as a function of R along the top of the grid. Once again $\Phi^{\mathcal{Q}}$ appears to be tracking the analytical solution extremely well, and $\Phi^{\mathcal{Y}}$ is seen to be converging toward $\Phi^{\mathcal{Q}}$ (and $\Phi^{\mathcal{A}}$) as the maximum

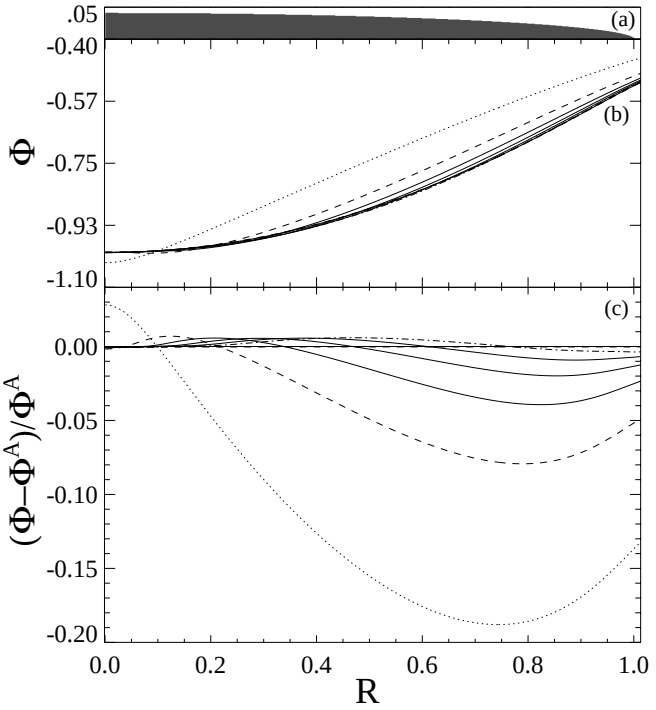

FIG. 3.—Model II (20:1 oblate spheroid); results from test 3, as defined in Table 2. (*a*) Meridional cross section through model II is shown in which the equatorial radius of the object extends to $R = 1.0$ and the polar radius extends to $Z = 0.05$. The top and right-hand edges of this figure frame illustrate precisely the positioning of the top and side boundaries of the 1024 × 64 cylindrical computational mesh have been positioned, relative to the highly flattened spheroidal surface. (*b*) Gravitational potential Φ is plotted as a function of R along the top boundary of the computational mesh, as determined analytically (*thin solid curve*), via the CCGF technique (*thick dashed curve*), and via the standard multipole technique as the limiting number of terms in the multipole expansion is increased successively by 2 from $l = 0$ (*dotted curve*) to $l = 2$ (*dashed curve*), etc., through $l = 10$ (*dot-dashed curve*). (*c*) Similar to Figs. 2*a* and 2*c*; the fractional error in the numerically determined gravitational potential relative to the analytically known potential $\Phi^{\mathcal{A}}$ is shown as a function of position R along the top of the selected cylindrical computational mesh. These fractional errors have been derived directly from the values of Φ displayed in (*b*), and the meaning of the various curves is the same as in (*b*). Note, in particular, that at all radii the error in $\Phi^{\mathcal{Q}}$ (*bold dashed curve*) is almost indistinguishable from zero.

number of terms in the multipole expansion is increased. However, for a given value of $l_{\max}$, the typical error in $\Phi^{\mathcal{Y}}$ appears to be larger for the prolate model (Fig. 4) than for the oblate model with the same aspect ratio (Fig. 3).

Figure 5 shows results for test 5 on model IV, an axisymmetric torus with a 20:1 aspect ratio. The information that has been displayed in the three panels of Figure 5 is analogous to the information that was displayed in Figure 3 for model II. Specifically, Figure 5*a* shows a meridional cross section through the torus, with the symmetry axis of the torus (and the cylindrical computational grid) at the left, while the top and right-hand edges of the frame identify precisely where the top and side cylindrical boundaries were placed with respect to the surface of the torus. In this case we do not have an analytical solution for the potential against which to compare $\Phi^{\mathcal{Y}}$ or $\Phi^{\mathcal{Q}}$, but in Figure 5*b* it is clear that as $l_{\max}$ is increased $\Phi^{\mathcal{Y}}$ is converging toward $\Phi^{\mathcal{Q}}$ (*thick-dashed curve*), so in Figure 5*c* the error in $\Phi^{\mathcal{Y}}$ has been measured relative to $\Phi^{\mathcal{Q}}$.

For test 6 we have returned to model I to illustrate how the calculated error in $\Phi^{\mathcal{Q}}$ improves with increasing compu-

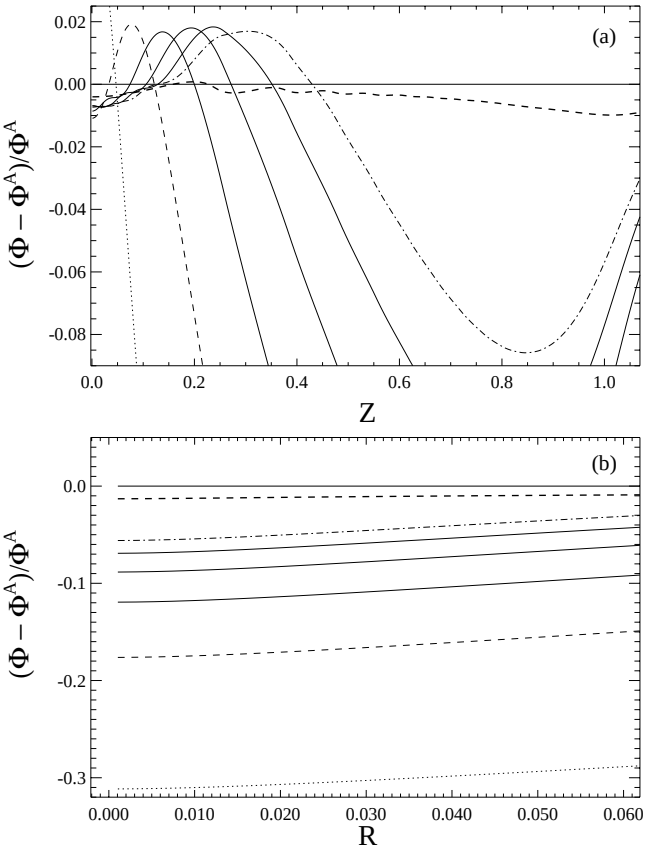

FIG. 4.—Model III (20:1 prolate spheroid); results from test 4, as defined in Table 2. (*a*) Analogously to Figs. 2*b* and 2*d*, the fractional error in the numerically determined gravitational potential relative to the analytically know potential Φ^A is shown as a function of position Z along the side boundary of the selected cylindrical computational mesh. (*b*) Analogously to Figs. 2*a*, 2*c*, and 3*c*, the fractional error in the numerically determined gravitational potential relative to the analytically known potential Φ^A is shown as a function of position R along the top boundary of the selected cylindrical computational mesh.

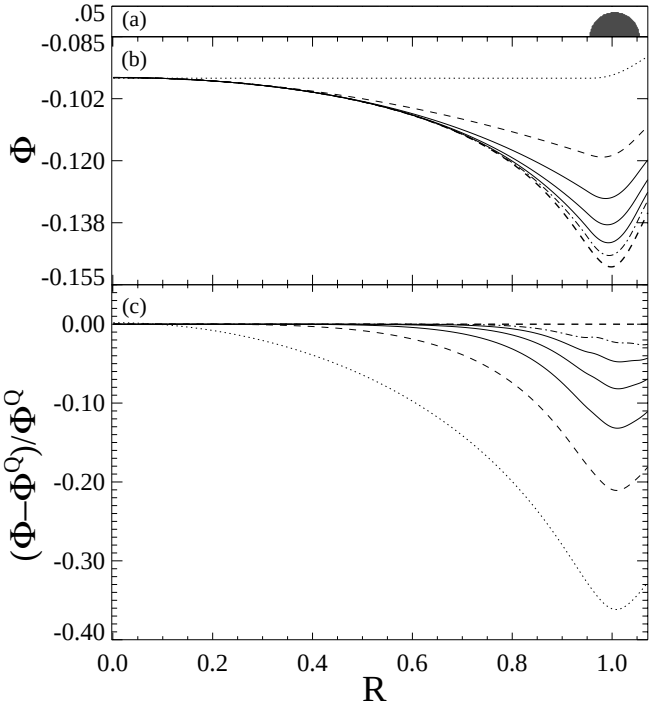

FIG. 5.—Model IV (20:1 torus); results from test 5. (*a*) Analogous to Fig. 3*a*; a meridional cross section through model IV in which the major and minor radii of the torus are 1.0 and 0.05, respectively. The top and right-hand edges of this figure frame illustrate precisely the positioning of the top and side boundaries of the 512 × 32 cylindrical computational mesh have been positioned, relative to the surface of the slender torus. (*b*) Analogously to Fig. 3*b*, the gravitational potential Φ is plotted as a function of R along the top boundary of the computational mesh, as determined via the CCGF technique (*thick dashed curve*), and via the standard multipole technique as the limiting number of terms in the multipole expansion is increased successively by 2 from $l = 0$ (*dotted curve*) to $l = 2$ (*dashed curve*), etc., through $l = 10$ (*dot-dashed curve*). (*c*) Analogous to Fig. 3*c*, but because the potential exterior to a torus is not known analytically, the fractional error in the numerically determined gravitational potential is shown here relative to the potential Φ^Q as determined from the CCGF technique. The meaning of the various curves is the same as in (*b*).

tational grid resolution. As indicated in Table 2, for this test we have computed the value of the potential on the boundary of 25 different sized grid meshes, all of which are integer multiples of a 32 × 8 cylindrical (R, z) grid. As is explained in detail in the figure caption, Figure 6*a* illustrates how the maximum, minimum, and mean fractional error in Φ^Q vary along the top boundary of the cylindrical grid as the radial grid resolution is increased from $J = 32$ to $J = 608$, and Figure 6*c* illustrates how the maximum, minimum, and mean fractional error in Φ^Q vary along the side boundary of the cylindrical grid as the vertical resolution is increased from $K = 32$ to $K = 200$. Along both the top and side boundaries we have been able to achieve mean fractional errors $\sim 10^{-5}$. For five selected grid resolutions (labeled B, C, D, E, and F in each frame of Fig. 6), we also have shown in detail how the fractional error in Φ^Q varies across the top (Fig. 6*b*) and along the side (Fig. 6*d*) boundaries of the grid. The curves in Figure 6*b* (or Fig. 6*d*) should each be compared directly with the thick-dashed curve plotted in Figure 2*b* (or Fig. 2*d*), which presents the equivalent information from test 2—a relatively low-resolution (128 × 32) but otherwise identical calculation that also shows up and is labeled "A" in the results of test 6.

We should point out that the fractional errors presented in Figure 6 for test 6 have all been calculated in a slightly different manner from the fractional errors that have been presented for tests 1–5. Before comparing Φ^Q to Φ^A in test 6, we have renormalized the total mass that has been used in the determination of Φ^A to correspond with the total mass that results from a discretization of model I inside our cylindrical computational grid of the specified ($J \times K$) resolution. As explained earlier in the context of tests 1 and 2, the thick-dashed curves in Figure 2 are slightly offset from zero primarily because of a slight discrepancy in mass that arises from trying to map a perfect spheroid onto a cylindrical coordinate mesh. By adjusting the mass that is being used in the analytical determination of the gravitational potential for model I to account for this discrepancy, we are able to present the fractional errors in such a way that they asymptotically approach zero at the largest illustrated values of R (Fig. 6*b*) and z (Fig. 6*d*). We also suspect that geometric imperfections arising from the discretization of the flattened spheroid are also responsible for the fact that the typical fractional errors shown in Figures 6*a* and 6*c* level out at around 10^{-5} and do not continue to decrease with increasing grid resolution.

3.2.2. *A Nonaxisymmetric Model*

In an effort to illustrate how well the CCGF method works for nonaxisymmetric mass distributions, we have

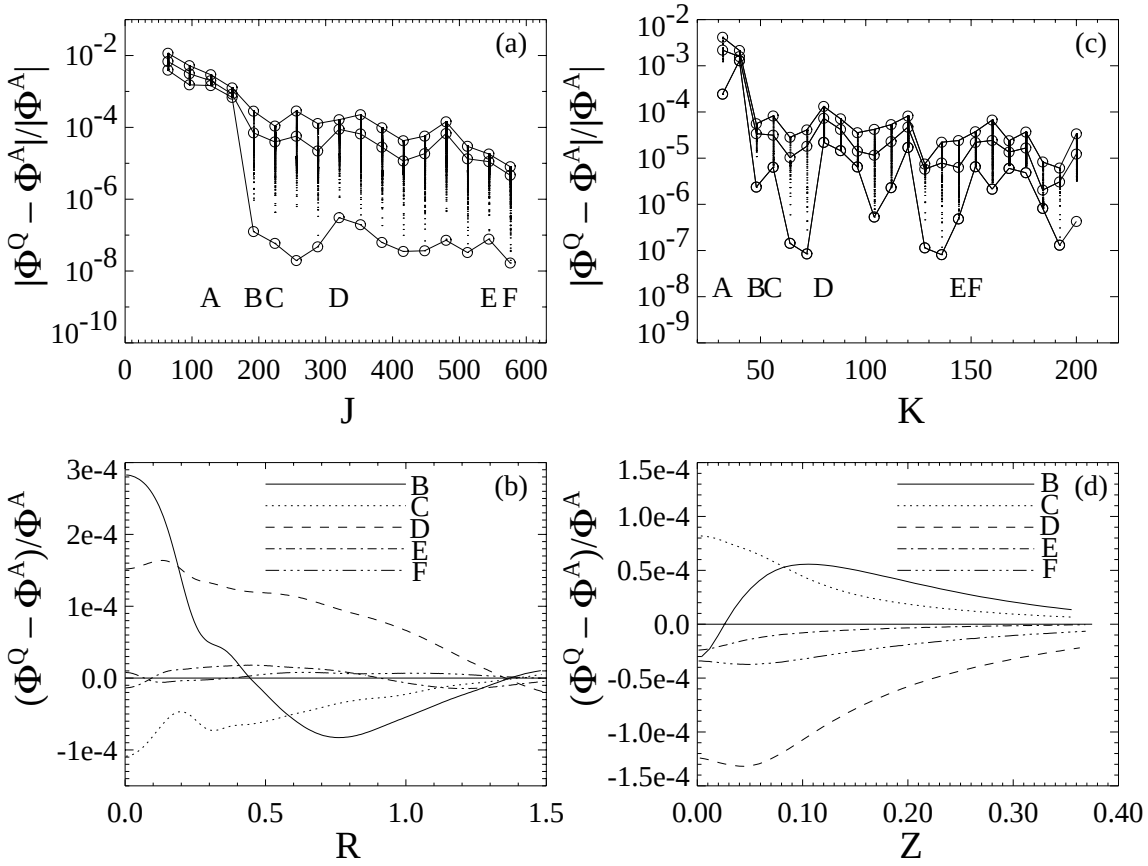

FIG. 6.—Model I (5:1 oblate spheroid); results from test 6. Fractional errors in the gravitational potential derived via the CCGF technique using 25 different cylindrical grid resolutions (see Table 2) to resolve the oblate spheroidal mass distribution. (*a*) For a specified radial grid resolution J, the vertical column of dots identifies on a logarithmic scale the full range of fractional errors that have been derived along the top boundary of the computational mesh. Each dot identifies the fractional error at a specific radial grid location so, for example, for the column of dots (labeled "A") that is drawn from a calculation using a grid resolution $J = 128$ (as in test 2; see also Fig. 3), 128 different dots have been plotted showing errors that range from 1.5×10^{-6} to 2×10^{-3}. At each grid resolution J, an open circle has been drawn to identify the largest, smallest, and median error; a solid line connecting the circles helps the eye recognize an overall trend in computed errors as the resolution of the model is improved. (*b*) Analogous to the thick dashed curve in Fig. 2*c*, the fractional error in the gravitational potential determined via the CCGF technique Φ^Q relative to the analytically known potential Φ^A is shown as a function of position R along the top of the selected cylindrical computational mesh, but for several different grid resolutions. The curves labeled B through F are drawn from models having the grid resolutions J as indicated by the corresponding column labels in (*a*). (*c* and *d*) Same as (*a*) and (*b*), respectively, but showing fractional errors that have been derived along the side boundary of the computational mesh from calculations using various vertical grid resolutions K (see Table 2).

developed a test based on the analytically known potential exterior to a triaxial homogeneous ellipsoid, as given in Appendix B by equation (B7). Specifically, as detailed in Tables 1 and 2 for test 7, we have embedded a homogeneous triaxial ellipsoid with a 20:10:1 axis ratio in a uniformly zoned cylindrical mesh with $512 \times 32 \times 256$ zones in the R, z, and ϕ directions, respectively. Test 7 is similar to test 3 in the sense that the top and side boundaries of the computational grid were positioned just outside the surface of the ellipsoid in such a way that a vertical cross section through the configuration that contains the major and minor axes of the ellipsoid looks identical to Figure 3*a*. As a result, a vertical cross section containing the minor and intermediate axes of the ellipsoid would show that, in the equatorial plane of the grid, the ellipsoidal surface extends only halfway out to the side boundary of the computational grid. Hence, we should expect any numerical evaluation of the potential on the top and side boundaries of our cylindrical grid to produce better results at azimuthal angles near the intermediate axis of the ellipsoid (i.e., near $\phi = \pi/2$ and $3\pi/2$) than at azimuthal angles near the ellipsoid's major axis ($\phi = 0$ and π; see Fig. 7*b*, below).

The analytical potential outside of a homogeneous, triaxial ellipsoid contains an infinite number of azimuthal Fourier components. When the ellipsoid is discretized and placed inside of a grid with a finite number of azimuthal zones, L (in our case, $L = 256$), we know by Fourier's Theorem that the "exact" potential corresponding to this discretized object will exhibit, at most, Fourier components extending up to mode $m = L/2$ (in our case, $m = 128$). As we have shown in § 2.2.1 (specifically, eq. [20]), via the CCGF method the amplitude and phase of each one of these Fourier modes can be determined precisely by performing a single integral over the mass distribution, weighted by the appropriate special function, $Q_{m-1/2}(\chi)$. In contrast to this (see § 2.1), when the method of multipole moments is employed, each of the azimuthal Fourier modes can be determined exactly only via a summation over an infinite number of terms ($l = 0$ to ∞), each one of which requires a separate integral over the mass distribution. Hence, by analogy with our determination of the axisymmetric potential, the multipole method can be implemented in the context of nonaxisymmetric mass distributions only if the l summation is truncated to a finite number of terms for each separate azimuthal Fourier mode. In a practical implementation of either method, it is computationally prudent to limit the calculation of Fourier mode amplitudes to a number substantially smaller than $m = L/2$, in which case

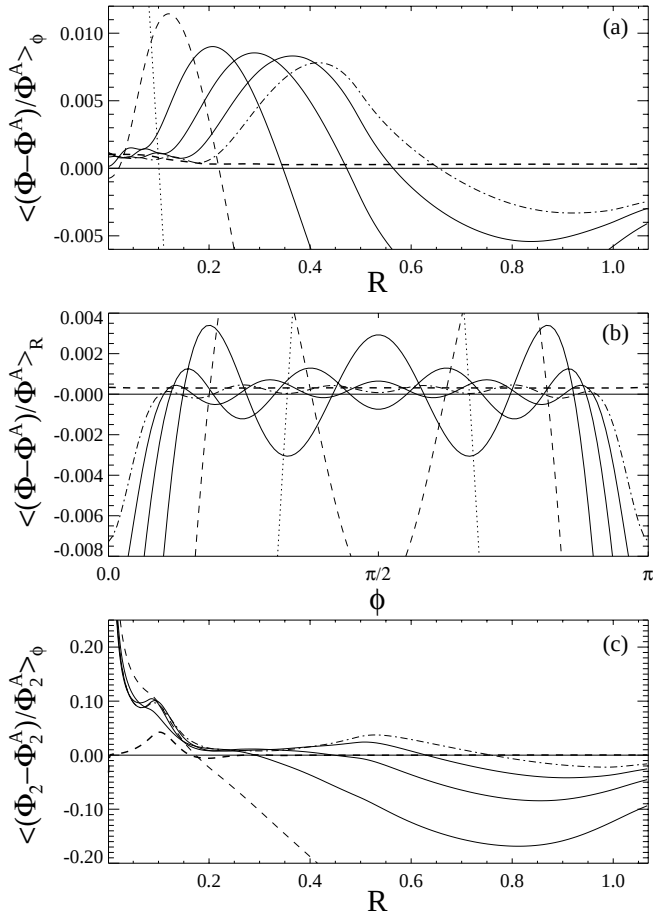

FIG. 7.—Model V (20:10:1 triaxial ellipsoid); results from test 7. (*a*) Analogous to Fig. 3*c*, except that, at each radius, the fractional error has been derived from an azimuthal average because model V is not an axisymmetric configuration. (*b*) In an effort to display information that is complementary to the results shown in (*a*) for this nonaxisymmetric configuration, the fractional error in the derived potential is shown as a function of azimuthal angle ϕ. The displayed error has been derived from a radial average at each angular position. (*c*) The error in the $m = 2$ Fourier component of the potential is displayed as a function of R along the top boundary of the computational mesh. In all three frames, by analogy with Fig. 3*c*, fractional errors have been determined via the CCGF technique (*thick dashed curve*), and via the standard multipole technique as the limiting number of terms in the multipole expansion is increased successively by 2 from $l = 0$ (*dotted curve*) to $l = 2$ (*dashed curve*), etc., through $l = 10$ (*dot-dashed curve*).

one must admit that even the CCGF method can at best produce only an approximation to the "exact" discretized potential, but at least the CCGF method provides an accurate determination of the amplitude and phase of each of the included azimuthal Fourier modes whereas, by truncating the l summation, the multipole method cannot.

In conducting test 7, we have included in the evaluation of Φ^Y even terms through $l_{\max} = 10$ and, for each value of l, even azimuthal modes through $m = \pm l$. (All odd azimuthal moments of the mass distribution are guaranteed to be zero because model V exhibits a periodic symmetry about the azimuthal angle $\phi = \pi$ as well as about $\phi = 0$ or 2π.) Therefore, in our evaluation of the double summation in equation (5) to calculate Φ^Y in test 7, 36 separate terms have been included. In addition, we have had to evaluate an entirely independent set of 36 terms associated with the summation in equation (11) because, as in tests 2, 3, and 5, most of the zones along the top boundary of our computational grid had radial locations $r_B < a_1$, that is to say, at least some of the material enclosed by model V's ellipsoidal surface fell outside a sphere of radius r_B. In contrast to this, when evaluating Φ^Q at each grid boundary location via equation (19), we included only 16 terms, but these 16 terms permitted us to include azimuthal Fourier mode contributions to the potential up through mode $m = 30$ because the odd azimuthal modes were guaranteed to be zero.

Figures 7*a* and 7*b* show how closely our determination of Φ^Y and Φ^Q in test 7 come to matching the analytical potential Φ^A for model V. Rather than trying to display the errors in Φ^Y and Φ^Q at all grid boundary locations, Figure 7*a* displays azimuthally averaged errors as a function of R along the top of the computational grid and Figure 7*b* displays radially averaged errors as a function of ϕ over the same region. Being azimuthally averaged, the error measurements presented in Figure 7*a* do not tell us much that was not already apparent in our examination of the corresponding axisymmetric spheroid (see test 3 and, specifically, Fig. 3*c*). However, Figure 7*b* is clearly illustrating something new. It illustrates that the potential Φ^Q determined through the CCGF method (*thick-dashed line*) represents the azimuthal variation of the potential outside of the triaxial ellipsoid very accurately. We also see in Figure 7*b* that, as $l_{\max}$ is increased, Φ^Y approaches Φ^Q.

Finally, via a Fourier analysis of Φ^A, we have determined the correct amplitude as a function of radius of a single, isolated azimuthal mode, Φ_2^A, for model V, and in Figure 7*c* we have compared this function with the corresponding $m = 2$ Fourier mode amplitudes of Φ^Y and Φ^Q. As a point of reference, the $m = 2$ Fourier amplitude Φ_2^Q has been derived via the integral expression (58) given in § 3.1.5. Figure 7*c* shows in a somewhat cleaner manner than does Figure 7*b* that the CCGF method works as well for the determination of the gravitational potential of nonaxisymmetric mass distributions as it does for axisymmetric systems. At most radii, Φ_2^Q is almost indistinguishable from Φ_2^A. Note, however, that near the z-axis of the grid (i.e., near the polar axis of the ellipsoid), Φ_2^Q does differ from Φ_2^A by a few percent. This deviation almost certainly occurs because we have used only 32 vertical zones to resolve model V's highly flattened mass distribution. Hence, the upper surface of our discretized mass model does not reproduce well the smooth quadratic surface of the analytically defined ellipsoid. Similar, although lower amplitude, deviations can be found near the z-axis in Figure 2*c* (test 2), Figure 4*a* (test 4), and Figure 7*a*. Once again, it is fair to say that Φ_2^Q provides a more correct description of the gravitational potential for the discretized mass model than does Φ_2^A. This statement is supported by the fact that, as $l_{\max}$ is increased, Φ^Y is converging toward Φ^Q in Figures 7*a* and 7*c*, rather than toward Φ^A.

3.3. *Computational Demands*

Here we compare the computational demands of the multipole moment and CCGF methods. We do so not from the standpoint of a static problem whose solution need be determined only once, but from the standpoint of a dynamical problem in which the system's two- or three-dimensional density distribution is changing with time, in which case a solution to the gravitational potential must be frequently redetermined in order to ensure that the potential is at all times consistent with the density distribution.

We will assume that, during such an evolutionary simulation, the cylindrical computational grid and the positions

along the grid boundaries at which the potential $\Phi(\boldsymbol{x}_B)$ is to be determined do not change with time. Under this assumption, it is clear that, whichever Green's function method is being used, the terms included in the Green's function itself do not vary with time because these terms are functions of only the coordinates. Hence, the functions $Y_{lm}(\theta, \phi)$ (for the multipole moment method) or $Q_{m-1/2}(\chi)$ (for the CCGF method) need be calculated only once, as appropriate, for each grid cell location and stored in memory for reuse throughout a time-evolutionary calculation. The primary calculational cost associated with either Green's function method therefore has very little to do with the cost of evaluating various Y_{lm} or the $Q_{m-1/2}$ expressions. Instead, the cost is directly related to the number of integrals N over (moments of) the mass distribution that must be reevaluated each time the mass-density distribution of the evolving system is updated.

For a (two-dimensional) mass distribution that is axisymmetric, but that otherwise exhibits no special geometric symmetries, the multipole moment method includes $l_{\max} + 1$ terms in the Green's function expansion, whereas the CCGF method contains only one. However, because the argument χ of the special function $Q_{m-1/2}(\chi)$ is, itself, a function of the boundary coordinates (R, z), a separate moment of the mass distribution must be calculated for each grid boundary location. Hence, for the CCGF method, the number of moments $N^{\mathcal{Q}}$ that must be reevaluated each time the mass-density distribution changes is

$$N^{\mathcal{Q}} = 2J + K \,, \tag{62}$$

where, as in Table 2, J and K specify the radial and vertical grid resolutions, respectively, and the factor of 2 indicates that in general "J" boundary values must be determined along the bottom as well as along the top of the cylindrical grid. In contrast to this, the terms in the multipole moment (i.e., spherical coordinate Green's function) expansion are not explicitly functions of the boundary coordinates, so

$$N^{\mathcal{Y}} = l_{\max} + 1 \,. \tag{63}$$

Now, as discussed earlier, in order to achieve the same level of accuracy with the multipole moment method as can be achieved with the CCGF method, $l_{\max}$ must be set to ∞. However, if, in practice, one is satisfied with the level of accuracy achieved by setting $l_{\max}$ to a value $l_{\max} < (2J + K - 1)$, then $N^{\mathcal{Y}}/N^{\mathcal{Q}} < 1$, and one may conclude that the multipole method is computationally less expensive than the CCGF method.

However, this is not the full story. Even though the terms in the multipole moment expansion are not explicitly functions of the boundary coordinates, the limits on the volume integration for each moment of the mass distribution will be a function of the boundary coordinates unless every point $\boldsymbol{x}_B$ along the boundary of the computational grid is at a radial location r_B that is greater than all interior grid locations at which matter resides. (See the related discussion associated with eq. [10] in § 2.1.) Test 1 (see Figs. 2*a* and 2*b*) is the only test presented above for which this special condition was true. By setting $J = K$, we ensured that every point along the top boundary of our cylindrical grid was at a radial location r_B greater than the equatorial radius of the 5:1 oblate spheroid, so the number of separate moments of the mass distribution that had to be evaluated in test 1 was, indeed, $N^{\mathcal{Y}} = l_{\max} + 1$. However, as explained in § 2.1, for situations in which the boundary of the grid is positioned close to the surface of a flattened or elongated mass distribution, it is necessary to calculate a separate set of "interior" and "exterior" mass moments for the majority of boundary locations.

For example, for mass distributions that are flattened along the symmetry axis, as in our tests 2, 3, 5, and 6, boundary locations along the side of the grid do not require separate sets of mass moments, but most boundary locations along the top and bottom of the grid do. Hence,

$$N^{\mathcal{Y}} \approx 4J(l_{\max} + 1) \,, \tag{64}$$

where the extra factor of 2 comes from having to determine both interior and exterior moments for each value of l, as shown in equation (10). Therefore, $N^{\mathcal{Y}}/N^{\mathcal{Q}} \sim l_{\max}$, and the (less accurate) multipole moment method proves to be more expensive to implement computationally than the CCGF method.

For a nonaxisymmetric (three-dimensional) mass distribution, the CCGF method will require the same number of moments as in the axisymmetric case *for each separate azimuthal Fourier mode*. Hence, if the discrete Fourier series is truncated at mode number $m_{\max}$, the number of moments $N^{\mathcal{Q}}$ that must be reevaluated each time the mass-density distribution changes is

$$N^{\mathcal{Q}} = 2m_{\max} \times (2J + K) \,, \tag{65}$$

where the leading factor of 2 comes from the fact that each Fourier mode requires the determination of both an amplitude and a phase. In the optimum situation where the boundary of the computational grid is everywhere outside the mass distribution, in three dimensions the multipole moment method will require the evaluation of

$$N^{\mathcal{Y}} \approx \sum_{l=0}^{l_{\max}} (2l + 1) = (l_{\max} + 1)^2 \tag{66}$$

separate moments (unless the strategic decision is made to set $m_{\max} \neq l_{\max}$). In most situations, then, $N^{\mathcal{Y}}/N^{\mathcal{Q}}$ will be less than unity, as in the corresponding optimum axisymmetric case, but the ratio will be somewhat larger here.

Again, though, for situations in which the boundary of the grid is positioned close to the surface of a flattened or elongated mass distribution, the number of moments required for the multipole moment method climbs substantially. For example, for a flattened nonaxisymmetric mass distribution like the one examined above in connection with test 7

$$N^{\mathcal{Y}} \approx 4J \times \sum_{l=0}^{l_{\max}} (2l + 1) = 4J(l_{\max} + 1)^2 \,, \tag{67}$$

and the ratio $N^{\mathcal{Y}}/N^{\mathcal{Q}}$ becomes even larger than it was for the corresponding axisymmetric case. Hence, in connection with a broad range of astrophysically interesting, two- and three-dimensional fluid flow problems, we have found the CCGF method to be not only much more accurate but also less expensive to implement than the traditional multipole method.

One note of caution is in order. Because the argument χ of the special function $Q_{m-1/2}(\chi)$ is a function of both coordinates of the interior mass (R', z'), at the beginning of any time-evolutionary simulation, a two-dimensional array of "Q" values must be calculated at each location along the boundary of the grid and for each discrete Fourier mode m. Hence, although the expense associated with the calculation

of this global Q array can be confined to initialization routines, it must generally be a four-dimensional array having dimensions $\sim[J \times K \times m_{\max} \times (2J + K)]$. As a result, the CCGF method can be quite demanding in terms of storage space. Because for a given azimuthal mode number m the function $Q_{m-1/2}(\chi)$ is very smooth over the entire range of χ, it may prove to be more practical to store only $m_{\max}$ one-dimensional arrays that could be referenced by all boundary grid cells in which the particular $Q_{m-1/2}$ function has been evaluated at a reasonably large number and sufficiently wide range of discrete values of χ. Then, when performing its own evaluation of the moments of the mass distribution, each boundary cell could evaluate $Q_{m-1/2}(\chi)$ as needed via an interpolation within the discretized array. We have not yet implemented such a scheme, although as we begin to investigate problems having sizes larger than the one illustrated in test 7, above, we will probably need to do so.

4. SUMMARY

When studying the structure, stability and/or dynamical evolution of astrophysical systems, it often seems natural to adopt cylindrical coordinates because the systems being studied are either rotationally flattened (e.g., galaxies and protostellar disks) or elongated along an underlying axis of magnetic and/or rotational symmetry (e.g., jets and bipolar flows). When self-gravity is important in defining a system's structural and stability properties, however, cylindrical coordinates have not provided much of a modeling advantage in the past. This is because the familiar expression for the Green's function expansion in cylindrical coordinates—shown here in equation (13)—involves not only an infinite summation over all azimuthal modes but also infinite integrals over products of Bessel functions of various orders. Because it is not obvious at what level the Bessel function integrals should be truncated in order to achieve a desired degree of accuracy for arbitrary mass distributions—and Bessel functions, themselves, are not as easy to evaluate as trigonometric functions—researchers usually have adopted a Green's function expansion in terms of spherical harmonics (even though this expansion is not well suited to flattened mass distributions) or have employed Cartesian coordinates along with Fourier techniques (see Hockney & Brownrigg 1974; James 1977; Hohl & Zang 1979), which are able to remove the infinite periodicity in order to evaluate the gravitational potential of an isolated mass distribution. (See Villumsen 1985 for one notable counterexample, and the Robijn & Earn 1996 examination of the relative utility of several other orthogonal coordinate systems.) Spherical harmonics also have been the basis set of choice in analyses of nonradial modes of oscillation in rotationally flattened stars (Tassoul 1978).

In § 2.2, we have derived a much more compact expression for the Green's function in cylindrical coordinates, namely equation (15) or equation (17). Given that the analytical solution to the infinite integral permitting the derivation of equation (15) from equation (13) has been known for over 50 years (see discussion on p. 389 of Watson 1944 for a more detailed historical presentation), it is hard to believe that we are the first to discover this CCGF (compact cylindrical Green's function) expansion. However, we can find no evidence that this compact expression has previously been utilized by the astrophysics community, except in its axisymmetric form (see § 3.1.2).

When studying the dynamical evolution of self-gravitating fluid systems, we historically have used Φ^Y, i.e., the multipole method based on spherical harmonics, to specify values of the potential on the boundary of our computational grid (Tohline 1980; Durisen & Tohline 1985; Williams & Tohline 1988; Woodward, Tohline, & Hachisu 1994; Tohline & Hachisu 1990), as have numerous other groups (Black & Bodenheimer 1975; Norman & Wilson 1978; Boss 1980; Stone & Norman 1992; Boss & Myhill 1995; Müller & Steinmetz 1995; Yorke & Kaisig 1995). In the majority of these studies it has been advantageous for us to set the vertical size K of our cylindrical grid equal to the radial size J of the grid because, as illustrated and discussed in depth in § 3.2, relatively small errors in Φ^Y can be achieved with a relatively small number of terms in the multipole expansion when the top of a cylindrical grid is placed far above a flattened mass distribution. (Test 1, and Fig. 2 in particular, illustrates the type of grid that we have frequently used in the past.) However, when the choice is made to set $K = J$, a very large number of computational grid cells must be placed between the surface of a rotationally flattened mass distribution and the top boundary of the grid, i.e., in a region of space that contains little matter and therefore is relatively uninteresting, physically. In the context of every other aspect of our simulations, such as the time integration of the equations governing motion of the fluid and the determination of the gravitational potential at all grid points interior to the grid boundary, it would be much more advantageous computationally to select a grid resolution with $K \ll J$. As discussed and illustrated in § 3.2, the CCGF expansion provides an ideal method for numerically evaluating the gravitational potential of nonspherical, isolated mass distributions on such flattened cylindrical coordinate grids. It is generally less costly to implement and always more accurate than methods that rely upon the standard expansion in terms of spherical harmonics. We now routinely incorporate the CCGF method in our self-gravitating fluid simulations. As an extension of the work presented by Robijn & Earn (1996), this new compact expansion may also prove to be useful in analytical studies of the structure and stability of self-gravitating systems because the half-integer degree Legendre functions about which the new expansion is made seem to offer a natural set of basis functions to aid in the isolation and evaluation of system eigenmodes.

We are grateful to Dana Browne and his suggestion in 1994 to use a Gauss-Legendre integrator, which motivated our search for an analytic solution to the infinite integral. Thanks to John Cazes for incorporating and optimizing the CCGF technique in the HPF version of our CFD code. Thanks to Patrick Motl for his optimizing suggestion, which sped up the initialization part of the CCGF code drastically, as well as for implementing the CCGF technique in Fortran 90 with MPI. Thanks to Eric Barnes for motivational discussions on coordinate systems. We acknowledge support from the US National Science Foundation through grants AST 95-28424 and DGE 93-55007, the latter of which has been issued through the NSF's Graduate Traineeships Program and from NASA through grant NAG5-8497. This work also has been supported, in part, by grants of high-performance computing time on NPACI facilities at SDSC and UT, Austin, and through the PET program of NAVOCEANO DoD Major Shared Resource Center in Stennis, MS.

APPENDIX A

A USEFUL MODAL EXPANSION

Morse & Feshbach (1953; see the expression just above their eq. [10.3.79]) have presented the following useful relationship in connection with the integral representation of $Q_{m-1/2}$:

$$Q_{m-1/2}(\cosh\,\mu) = \frac{1}{2\sqrt{2}} \int_0^{2\pi} \frac{\cos\,(m\phi')\,d\phi'}{\sqrt{\cosh\,\mu - \cos\,\phi'}}\,. \tag{A1}$$

Multiplying both sides of this expression by $e^{im\,\phi}$ and then summing both sides from $m = -\infty$ to $m = \infty$ yields the following expression:

$$\sum_{m=-\infty}^{\infty} e^{im\,\phi} Q_{m-1/2}(\cosh\,\mu) = \frac{1}{2\sqrt{2}} \int_0^{2\pi} \frac{d\phi'}{\sqrt{\cosh\,\mu - \cos\,\phi'}} \sum_{m=-\infty}^{\infty} (e^{im(\phi+\phi')} + e^{im(\phi-\phi')})\,. \tag{A2}$$

Utilizing the following representation of the Dirac delta function (e.g., eq. [3.139] of Jackson 1975),

$$\delta(\Theta) = \frac{1}{2\pi} \sum_{m=-\infty}^{\infty} e^{im\,\Theta}\,, \tag{A3}$$

the integral on the right-hand side of equation (A2) can be readily performed, giving

$$\frac{1}{\sqrt{\cosh\,\mu - \cos\,\phi}} = \frac{\sqrt{2}}{\pi} \sum_{m=-\infty}^{\infty} e^{im\,\phi} Q_{m-1/2}(\cosh\,\mu)\,, \tag{A4}$$

or, written entirely in terms of real functions,

$$\frac{1}{\sqrt{\cosh\,\mu - \cos\,\phi}} = \frac{\sqrt{2}}{\pi} \sum_{m=0}^{\infty} \epsilon_m \cos\,(m\phi) Q_{m-1/2}(\cosh\,\mu)\,. \tag{A5}$$

APPENDIX B

SELECTED ANALYTICAL POTENTIAL-DENSITY PAIRS

For a distinguished class of nonspherical objects there exist analytical solutions for the Newtonian potential given in terms of elementary and special functions. Below we list a few of these distinguished objects and the analytical forms of the exterior potential associated with them. There is a long history associated with these problems (see, e.g., Ramsey 1981; Binney & Tremaine 1987). Unfortunately, these objects do not represent most of the types of objects for which one might need to calculate gravitational forces. Even so, they are certainly very useful in comparing numerical methods for evaluating potentials.

Consider a homogeneous, axisymmetric spheroid defined such that

$$\rho(R,\,z) = \begin{cases} \rho_0, & \text{if } R^2/a_1^2 + z^2/a_3^2 \le 1\,, \\ 0, & \text{if } R^2/a_1^2 + z^2/a_3^2 > 1\,, \end{cases} \tag{B1}$$

where a_1 and a_3 are the equatorial and polar radii of the spheroid, respectively. From Chandrasekhar (1969), we find that the gravitational potential exterior to the spheroid is

$$\Phi(R,\,z) = \pi G \rho_0\, a_1^2\, a_3 \left\{ \left[1 + \frac{R^2}{2(a_3^2 - a_1^2)} - \frac{z^2}{a_3^2 - a_1^2} \right] I_1 - \frac{R^2 \sqrt{a_3^2 + \lambda}}{(a_3^2 - a_1^2)(a_1^2 + \lambda)} - \frac{2z^2}{(a_1^2 + \lambda)\sqrt{a_3^2 + \lambda}} - \frac{2z^2 \sqrt{a_3^2 + \lambda}}{(a_3^2 - a_1^2)(a_1^2 + \lambda)} \right\} \tag{B2}$$

where

$$\lambda = [(R^2 + z^2 - a_1^2 - a_3^2) + \sqrt{(a_1^2 + a_3^2 - R^2 - z^2)^2 - 4(a_1^2\, a_3^2 - R^2 a_3^2 - z^2 a_1^2)}]/2\,, \tag{B3}$$

and, for an oblate spheroid ($a_1 > a_3$),

$$I_1 = \frac{\pi}{\sqrt{a_1^2 - a_3^2}} - \frac{2}{\sqrt{a_1^2 - a_3^2}} \tan^{-1} \sqrt{\frac{a_3^2 + \lambda}{a_1^2 - a_3^2}}\,, \tag{B4}$$

whereas for a prolate spheroid ($a_1 < a_3$),

$$I_1 = \frac{-1}{\sqrt{a_3^2 - a_1^2}} \ln \left[\frac{(\sqrt{a_3^2 + \lambda} - \sqrt{a_3^2 - a_1^2})^2}{a_1^2 + \lambda} \right]. \tag{B5}$$

For a homogeneous, triaxial ellipsoid defined such that

$$\rho(x, y, z) = \begin{cases} \rho_0, & \text{if } x^2/a_1^2 + y^2/a_2^2 + z^2/a_3^2 \le 1 , \\ 0, & \text{if } x^2/a_1^2 + y^2/a_2^2 + z^2/a_3^2 > 1 , \end{cases} \tag{B6}$$

where the three principal axes are defined such that $a_1 > a_2 > a_3$, the potential at any point $\boldsymbol{x} = (x, y, z)$ exterior to the ellipsoid is

$$\Phi(\boldsymbol{x}) = \frac{2\pi\rho_0 a_1 a_2 a_3}{\sqrt{a_1^2 - a_3^2}} \left\{ \left(1 - \frac{x^2}{a_1^2 - a_2^2} + \frac{y^2}{a_1^2 - a_2^2} \right) F(\theta, k) + \left[\frac{x^2}{a_1^2 - a_2^2} - \frac{(a_1^2 - a_3^2)y^2}{(a_1^2 - a_2^2)(a_2^2 - a_3^2)} + \frac{z^2}{a_2^2 - a_3^2} \right] E(\theta, k) \right.$$
$$\left. + \left(\frac{a_3^2 + \lambda}{a_2^2 - a_3^2} y^2 - \frac{a_2^2 + \lambda}{a_2^2 - a_3^2} z^2 \right) \frac{\sqrt{a_1^2 - a_3^2}}{\sqrt{(a_1^2 + \lambda)(a_2^2 + \lambda)(a_3^2 + \lambda)}} \right\} , \tag{B7}$$

where

$$F(\theta, k) = \int_0^\theta \frac{d\phi}{\sqrt{1 - k^2 \sin^2 \phi}} \tag{B8}$$

and

$$E(\theta, k) = \int_0^\theta d\phi \sqrt{1 - k^2 \sin^2 \phi} \tag{B9}$$

are Legendre's elliptic integrals of the first and second kind, respectively,

$$\theta \equiv \sin^{-1} \sqrt{\frac{a_1^2 - a_3^2}{a_1^2 + \lambda}} , \tag{B10}$$

$$k^2 \equiv \frac{a_1^2 - a_2^2}{a_1^2 - a_3^2} , \tag{B11}$$

and λ is defined as the algebraically largest root of the following cubic equation:

$$\frac{x^2}{a_1^2 + \lambda} + \frac{y^2}{a_2^2 + \lambda} + \frac{z^2}{a_3^2 + \lambda} = 1 . \tag{B12}$$

REFERENCES

Abramowitz, M., & Stegun, I. A. 1965, Handbook of Mathematical Functions with Formulas, Graphs, and Mathematical Tables (New York: Dover)
Arfken, G. 1985, Mathematical Methods for Physicists (New York: Academic)
Barnes, J., & Hut, P. 1986, Nature, 324, 446
Binney, J., & Tremaine, S. 1987, Galactic Dynamics (Princeton: Princeton Univ. Press)
Black, D., & Bodenheimer, P. 1975, ApJ, 199, 619
Boss, A. 1980, ApJ, 242, 699
Boss, A. P., & Myhill, E. A. 1995, Comput. Phys. Commun., 89, 59
Chandrasekhar, S. 1969, Ellipsoidal Figures of Equilibrium (New York: Dover)
de Zeeuw, T. 1985, MNRAS, 216, 273
Durisen, R. H., & Tohline, J. E. 1985, in Protostars and Planets II, ed. D. C. Black & M. S. Matthews (Tucson: Univ. Arizona Press), 534
Earn, D. J. D. 1996, ApJ, 465, 91
Evans, N. W., & de Zeeuw, P. T. 1992, MNRAS, 257, 152
Gradshteyn, I. S., & Ryzhik, I. M. 1994, Table of Integrals, Series, and Products (New York: Academic)
Hockney, R. W., & Brownrigg, D. R. K. 1974, MNRAS, 167, 351
Hohl, F., & Zang, T. A. 1979, AJ, 84, 585
Jackson, J. D. 1975, Classical Electrodynamics (New York: Wiley)
James, R. A. 1977, J. Comput. Phys., 25, 71
Kalnajs, A. 1971, ApJ, 166, 275
Landau, L. D., & Lifshitz, E. M. 1960, Electrodynamics of Continuous Media (Oxford: Pergamon Press)
Morse, P., & Feshbach, H. 1953, Methods of Theoretical Physics (New York: McGraw-Hill)
Müller, E., & Steinmetz, M. 1995, Comput. Phys. Commun., 89, 45
Norman, M., & Wilson, J. R. 1978, ApJ, 224, 497
Ramsey, A. S. 1981, Newtonian Attraction (Cambridge: Cambridge Univ. Press)
Robijn, F. H. A., & Earn, D. J. D. 1996, MNRAS, 282, 1129
Stone, J., & Norman, M. 1992, ApJS, 80, 753
Tassoul, J.-L. 1978, Theory of Rotating Stars (Princeton: Princeton Univ. Press)
Tohline, J. 1980, ApJ, 235, 866
Tohline, J. E., & Hachisu, I. 1990, ApJ, 361, 394
US. NBS. Comput. Lab. 1945, Tables of Associated Legendre Functions (New York: Columbia Univ. Press)
Villumsen, J. V. 1985, ApJ, 290, 75
Williams, H. A., & Tohline, J. E. 1988, ApJ, 334, 449
Woodward, J. W., Tohline, J. E., & Hachisu, I. 1994, ApJ, 420, 247
Watson, G. N. 1944, A Treatise on the Theory of Bessel Functions (Cambridge: Cambridge Univ. Press)
Yorke, W. H., & Kaisig, M. 1995, Comput. Phys. Commun., 89, 29

Note added in proof.—It has recently come to our attention that equation (A4) appears in problem (1) on p. 465 of H. Bateman (Partial Differential Equations of Mathematical Physics [1959; Cambridge: Cambridge Univ. Press]; also see E. Heine, Handbuch der Kugelfunctionen, Theorie und Anwendungen, 2, umgearb. und verm. Aufl., 2 vols [1881; Berlin: G. Reimer], p. 286) in the context of toroidal coordinates. This confirms our suspicion that the functional form of our CCGF had previously been derived, but the result has remained unfamiliar to the astrophysics community and does not appear to have been used previously in the context of circular cylindrical coordinates.